Additive Manufacturing and Spark Plasma Sintering of Lunar Regolith for Functionally Graded Materials

Laot, M.A.L.; Rich, Belinda; Cheibas, Ina ; Fu, J.; Zhu, Jia-Ning; Popovich, V.

DOI
10.7480/spool.2021.2.5258

Publication date
2021

Document Version
Final published version

Published in
Spool. Journal of Architecture and the Built Environment

Additive Manufacturing and Spark Plasma Sintering of Lunar Regolith for Functionally Graded Materials

Mathilde Laot [1], **Belinda Rich** [2], **Ina Cheibas** [2], **Jia Fu** [1], **Jia-Ning Zhu** [1], **Vera A. Popovich** [1]

[1] **Delft University of Technology**
Department of Materials Science and Engineering
Delft, the Netherlands

[2] **ESA/ESTEC European Space Agency**
Noordwijk, the Netherlands

Abstract

This study investigates the feasibility of in-situ manufacturing of a functionally graded metallic-regolith. To fabricate the gradient, digital light processing, an additive manufacturing technique, and spark plasma sintering were selected due to their compatibility with metallic-ceramic processing in a space environment. The chosen methods were first assessed for their ability to effectively consolidate regolith alone, before progressing to sintering regolith directly onto metallic substrates. Optimized processing conditions based on the sintering temperature, initial powder particle size, and different compositions of the lunar regolith powders were identified. Experiments have successfully proven the consolidation of lunar regolith simulants at 1050°C under 80 MPa with digital light processing and spark plasma sintering, while the metallic powders can be fully densified at relatively low temperatures and a pressure of 50 MPa with spark plasma sintering. Furthermore, the lunar regolith and Ti_6Al_4V gradient was proven to be the most promising combination. While the current study showed that it is feasible to manufacture a functionally graded metallic-regolith, further developments of a fully optimized method have the potential to produce tailored, high-performance materials in an off-earth manufacturing setting for the production of aerospace, robotic, or architectural components.

Keywords

In-Situ Resource Utilization (ISRU), Regolith, Functionally Graded Materials (FGM), Additive Manufacturing (AM), Digital Light Processing (DLP), Spark Plasma Sintering (SPS)

DOI

https://doi.org/10.7480/spool.2021.2.5258

Introduction

Lunar exploration is an essential step for long-term space expeditions. The Moon is exceptionally advantageous compared to other planetary bodies because of its proximity and fast communication times with Earth (Benaroya, 2018). It can serve as a strategic cornerstone of future technological developments in aerospace science and engineering, physics, and other disciplines (Eckart, 1999). Lunar infrastructure, such as space habitats and engineering tools, are critical for a successful mission. They must ensure high mechanical performance and safety against the harsh environmental conditions, such as radiation, meteoroids, thermal fluctuations, and ultra-high vacuum (Howe & Sherwood, 2009; Naser & Chehab, 2018). Furthermore, the ideal infrastructure would be autonomous, with build in-situ capabilities to substantially diminish the weight of payload brought from Earth (Frank et al., 2013). Thus, manufacturing proposals use local resources to design resilient and affordable human and robotic exploration tools. In-situ resource utilization (ISRU) is a key strategy for manufacturing space habitats and components (Kennedy, 2002; Sanders et al., 2005). Lunar soil or regolith is the primary material for ISRU and is most abundant on the Moon. Regolith is an abrasive and corrosive powder that contains several silicates (plagioclase, feldspar, pyroxene, olivine) and oxide minerals (ilmenite, spinel), see Table 1 (Edmunson & Rickman, 2012; Papike et al., 1982). These silicates and oxide minerals are abundant in metals such as silicon (Si), aluminium (Al), iron (Fe), titanium (Ti), and magnesium (Mg) (Mueller et al., 1988; Pieters, 1986; Prettyman et al., 2006; Taylor, 1987). The metals can be extracted by pyrometallurgy, electrometallurgy, and hydrometallurgy methods, with oxygen resulting as a by-product of this refining process (Agosto, 1981; Allen et al., 1996; Landis, 2007). However, metallic powders have not yet been investigated for lunar infrastructure fabrication. Current research focuses largely on the automated fabrication of structures from regolith simulants, which does not take full advantage of the ISRU potential.

The predominant construction approach for a permanent Moon base is additive manufacturing (AM). AM is divided into several families, namely material extrusion, material jetting, binder jetting, stereolithography or digital light processing, powder bed fusion, and direct energy deposition (F42 Committee, n.d.; Labeaga-Martínez et al., 2017). These AM methods are generally selected based on their technological feasibility for a lunar scenario and their expected performance (Dordlofva & Törlind, 2017). Material extrusion and binder jetting are promising techniques that use water with regolith in a concrete slurry (Cesaretti et al., 2014; Khoshnevis et al., 2005; Pilehvar et al., 2020). The disadvantages of these methods, however, include the large amount of water used, which is a highly scarce resource and valuable in space. Other fabrication methods are solar sintering and powder bed fusion, which involve the sintering of lunar regolith using solar light (Fateri, Meurisse, et al., 2019). Meurisse et. al. (2018) demonstrated the concept by manufacturing the first solar 3D-printed brick with lunar regolith simulant. This technique illustrates potential to use AM to build habitats or roads prior to astronaut' arrival (Fateri, Pitikaris, et al., 2019). Nevertheless, the vast majority of these studies employ components with inadequate mechanical properties (Goulas et al., 2018). The materials exhibit limited compressive or tensile strength and are not able to overcome the multitude of environmental requirements in space (Cesaretti et al., 2014; Goulas et al., 2017; Goulas & Friel, 2016; Meurisse et al., 2017; Neves et al., 2020). Such environmental factors include solar energetic particles (SEP), galactic cosmic rays (GCR), abrasion, wear, thermal fluctuations, refrigeration, ultra-high vacuum, resistance to fatigue, impact and pressurization, meteoroids and mechanical impacts, and biological and chemical inertness (Vaniman et al., 1991). Therefore, there is a need for resilient composites that can overcome all these environmental parameters and take full advantage of the potential of ISRU.

Functionally graded materials (FGM) are high-performance composites designed to achieve tailored features (Bever & Duwez, 1972). FGM can overcome the multitude of lunar requirements with functions or performance embodied in a graduated morphology. These materials are advantageous for maximizing ISRU capabilities due to their multi-material approach, which is high performance relative to monolithic

applications (Kim & Na, 1995; Srivastava et al., 2019; Suresh & Mortensen, 1997). FGM can improve mechanical behaviour via a specific distribution of materials in a graded layer. Several metal-ceramic gradients have been widely studied in recent years because of their highly attractive properties, such as high-temperature stability, high hardness, corrosion resistance, and versatility (Balla et al., 2007; Gong et al., 2018; Jin et al., 2018; Kamaruzaman et al., 2018; Katz-Demyanetz et al., 2019; Maseko et al., 2018; Popovich et al., 2018; Restivo et al., 2019; X. Zhang et al., 2018). A regolith to metal gradient can potentially be manufactured to combine ceramic-like properties with metal-like mechanical behaviour (Jin et al., 2018; Kamaruzaman et al., 2018). Such materials are expected to demonstrate improved resistance to thermal fatigue over conventional interfaces due to their graduated nature (Restivo et al., 2019), a crucial requirement for the dramatic thermal cycles experienced on the lunar surface, as well as high overall fracture toughness due to the presence of intermediate metallic-ceramic phases (Rattanachan et al., 2003). Compressive strength is expected to be in line with other regolith consolidation methods, in the range of 2 to 10 MPa (Altun et al., 2021).

The manufacturing technique plays an essential role in achieving such a gradient. Previous research investigated the powder characterization of regolith simulants to determine the feasibility of using AM to produce FGMs (Cheibas et al., 2020). Chemical composition, thermal characteristics, particle shape, and size distribution of the powders were analysed to determine regolith processability. This study found that digital light processing (DLP) and spark plasma sintering (SPS) are compatible consolidation techniques for both ceramic and metal powders, and thus FGMs (C. Zhang et al., 2019; Liu et al., 2019; Balla et al., 2012). Furthermore, preparation of the lunar simulant, particularly sieving and crushing, is necessary before consolidation due to the large particle size and shape.

Materials and methods

Powder characterisation

Three regolith simulants were evaluated for manufacture of a functionally-graded metallic-regolith: EAC-1A, LHS-1 (Lunar Highlands Simulant) and LMS-1 (Lunar Mare Simulant). The EAC-1A simulant was sourced from the European Astronaut Centre, Cologne, Germany, while LHS-1 and LMS-1 simulants were sourced from the CLASS Exolith Lab, Orlando, USA (CLASS Exolith Lab, n.d.-a; Engelschiøn et al., 2020). The use of simulant powders is necessary due to the limited availability of lunar soil. Thus, some differences between the terrestrial simulants and the actual lunar material are to be expected. Table 2 shows the similarity in oxide and mineralogical compositions between the chosen simulants and lunar Apollo samples. The element compositions of suite soils from the Apollo landing sites differ depending on the area of extraction: maria or highlands. The Apollo maria samples are similar to the LMS-1 simulant, with a higher concentration of titanium (Ti), ferrous oxides (FeO), and lower concentration of aluminium (Al). The highlands samples have a lower titanium (Ti) and iron (Fe) concentration, and higher aluminium in (Al) and calcium (Ca), similar to the LHS-1 simulant. The dominant mineralogical lunar content both for mare and highlands rock type is basaltic. The lunar highlands however, are more chemically simplified than the mare basalts. The highlands have different textural relationships dependent upon the degree of melting and recombination with other mineralogical components. Furthermore, essential differences exist between the Moon and Earth basalts. The key mineralogical difference in the lunar samples is the presence of FeO and Fe^{2+}, compared to terrestrial materials that typically consist of Fe^{2+} and Fe^{3+}.

	EAC-1A	LHS-1	LMS-1	MODAL PROPORTIONS
Plagioclase	17.0	32.8	74.4	12.9 – 69.1
Glass Mare	-	-	24.2	0.9 – 17.2
Glass Highlands	-	24.5	-	3.8 – 25.0
Basalt	-	19.8	0.5	-
Ilmenite	-	11.1	0.4	0.0 – 12.8
Pyroxene	22.0	7.5	0.3	8.5 – 61.1
Olivine	14.0	4.3	0.2	0.2 – 17.5
Iron Oxide	13.0	-	-	-
Other	8.0	-	-	-
Total	**74.0**	**100**	**100**	

TABLE 1 Summary of mineralogical content (in wt.%) of three lunar regolith simulants (EAC-1A, LHS-1 and LMS-1) compared to the average volume percentages collected at the Apollo and Luna sites (Brown et al., 1975; Eckart, 1999).

	EAC-1A	LHS-1	LMS-1	APOLLO MARIA	APOLLO HIGHLAND
SiO_2	43.70	44.18	42.18	45.4	45.50
TiO_2	2.40	0.79	4.62	3.90	0.60
Al_2O_3	12.60	26.24	14.13	14.90	24.00
Cr_2O_3	-	0.02	0.21	-	-
Fe_2O_3	12.00	-	-	-	-
FeO	-	3.04	7.87	14.10	5.90
MgO	11.90	11.22	18.89	9.20	7.50
MnO	0.20	0.05	0.15	-	-
CaO	10.80	11.62	5.94	11.80	15.90
Na_2O	2.90	2.30	4.92	0.60	0.60
K_2O	1.30	0.46	0.57	-	-
SO_3	-	0.10	0.11	-	-
Total	**98.40**	**100**	**99.56**	**99.9**	**100**

TABLE 2 Oxide composition (given in wt.%) of three lunar regolith simulants (EAC-1A, LHS-1 and LMS-1 (Cannon, n.d.-a; Cannon, n.d.-b. Schleppi et al., 2018)) and the average of the lunar surface samples from Apollo maria and highlands regions (Mueller et al., 1988; Sibille et al., 2006).

Figure 1 (a) shows the particle size distribution of each simulant. All simulants exhibit a wide particle size range, namely 0.02 µm - 2000 µm for EAC-1A and <1 µm - 1000 µm for LHS-1 and LMS-1. The mean particle size is 10.5 µm for EAC-1A, 94 µm for LHS-1, and 63 µm for LMS-1 (CLASS Exolith Lab, n.d.-b; CLASS Exolith Lab, n.d.-c; Manick et al., 2018). The significant large grain fraction was predicted to cause difficulty in additive manufacturing, particularly in densification during sintering. Due to this, all three simulants underwent sieving through 50 or 100 µm mesh sieves to allow better sintering. A 30g batch of EAC-1A was milled in a Retsch planetary ball mill in an argon atmosphere using tungsten carbide balls (5 and 10 mm). The powder was milled for 30 hours at a speed of 300 rpm with a ball to powder mass ratio of 10:1. The contamination was kept very low, and the maximum particle size was reduced to 22 µm with mean particle size of 5 µm. Figure 1 (b) shows X-ray diffraction (XRD) patterns for all three lunar regolith simulants and confirms the presence of plagioclase, pyroxene. and iron oxide. Cheibas et al. conducted combined differential scanning calorimetry (DSC) and thermogravimetric analysis (TGA) to characterise the thermal behaviour of the given simulants (Cheibas et al., 2020). It was found that all three simulants exhibited a thermal transformation in the 1100°C - 1500°C temperature range, indicating partial melting taking place at these temperatures. Mass losses ranging from 0.97% to 2.75% were also observed in the simulants at temperatures above 1350°C, which is attributed to the loss of volatiles from the powder.

Regarding metal, several elements such as titanium, iron, and aluminium are abundant in lunar soil. Pure metallic powders have the potential to be extracted on the Moon and used to fabricate FGM. However, this research is a first step to determine the feasibility of a functionally graded regolith-metallic substrate. Due to the novelty of this study, an investigation is necessary to determine if the interface between the regolith and a terrestrial AM metallic powder is possible. Stainless steel 316L and Ti_6Al_4V are high-grade metallic powders, frequently used in the aerospace industry for AM techniques (Mertens et al., 2014). These powders are selected because of their proven FGM potential and enhanced mechanical properties (Karami et al., 2020; Ruys et al., 2001). Therefore, in this study, the metallic powders used are stainless steel 316L and Ti_6Al_4V. The stainless steel powder was provided by Admatec (Alkmaar, The Netherlands) with a particle size range of <1 to 30 µm. The powder contains mainly austenite with a small portion of ferrite. Ti_6Al_4V powder was provided by AP&C advanced powder & coatings, with a particle size range of 15 to 45 µm. The powder is composed solely of the alpha phase, an HCP lattice of Ti_6Al_4V.

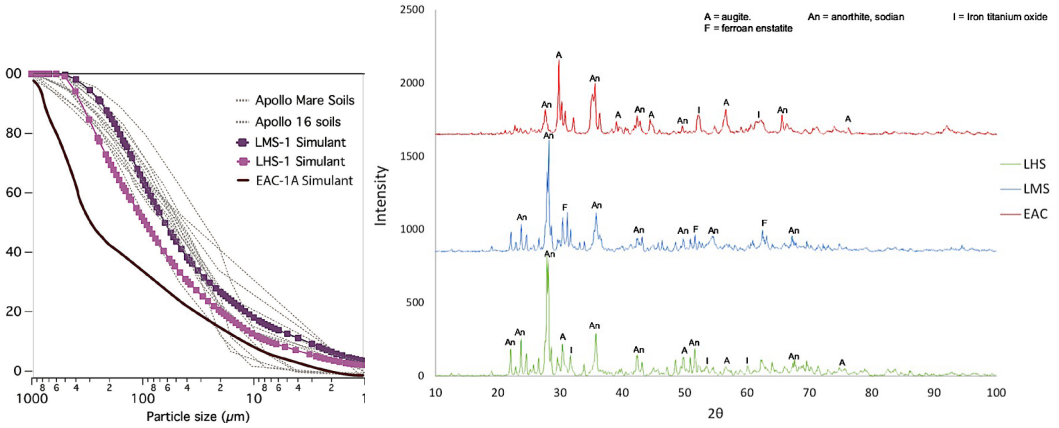

FIGURE 1 a) Average particle size distribution for EAC-1A, LHS-1 and LMS-1. Apollo data is shown for comparison and has been adjusted to remove the >1mm fraction. b) XRD patterns of the 3 lunar regolith simulants powders.

Additive manufacturing consolidation techniques

Stereolithography, powder bed fusion, and direct energy deposition are AM methods able to process metal powders. However, the fabrication of functionally graded metallic-regolith has to be compatible with both the metal powders and lunar regolith. In the case of powder bed fusion and direct energy deposition, the current hardware to control a robust graded multi-material deposition is limited. Stereolithography, namely digital light processing (DLP), however, has the potential to achieve a metallic-regolith gradient and has been proven to work with lunar simulants (Altun et al., 2021). Therefore, DLP has a higher probability of success in consolidating the regolith and FGM as a proof of concept.

The DLP method is a liquid-based AM technique able to fabricate complex three-dimensional structures from ceramic or metallic powders. This vat polymerization method uses ultraviolet (UV) light to harden or cure a photopolymer resin. Meanwhile, a platform moves upward or downward after each new layer of the 3D printed object is cured (Chua et al., 2017; Zheng et al., 2012). The DLP method is divided into three steps: 1) printing the 3D model into the required shape; 2) debinding, to remove the polymeric binder; and 3) sintering as a final step aimed at full consolidation.

There are certain features of DLP which makes it incompatible with a lunar environment, such as scarcity and outgassing of the resin. A plausible scenario is to replace the conventional resin with a bio-inspired alternative to adapt this AM method to lunar infrastructure (Shiwei et al., 2020). Furthermore, the debinding step must be optimised for vacuum to prevent defect formation, which may occur when volatile products are unable to effectively escape the green body. This is more likely to occur in vacuum debinding than air debinding due to higher activation energy for binder degradation processes (Wright et al., 1989). Nonetheless, resin and debinding development is outside of the scope of this research.

In this study, DLP was performed using the EAC-1A powder. The original powder was sieved through a 30 µm sieve and the content of lunar regolith powder of the slurry was set to 41%. Rectangular bars were 3D-printed with a layer thickness of 50 µm and a depth of cure of 100 µm. Water debinding was performed for 1 day followed by debinding in a furnace. Debinding in the furnace involved slow heating in air with stops at 150, 300, 400, and 600°C to obtain the optimal removal of the resin and to reduce the remaining carbon as much as possible. The bars were then sintered in a standard furnace in an air atmosphere. The first sintering temperature was set to 1050°C and kept for 1 hour, with a slow heating rate of 100°C/h. An additional sintering run at 1075°C was carried out to improve sintering of the bars.

Printing and debinding were successfully performed in the DLP process. However, the standard sintering step required further optimisation to obtain good densification. Spark plasma sintering was then introduced to optimise the sintering parameters.

Spark plasma sintering (SPS) is a manufacturing technique that utilizes uniaxial pressure and pulsed or unpulsed DC or AC current to consolidate powders into the required shape (Munir et al., 2006). SPS has been previously studied as a technique to consolidate lunar regolith simulants, metal powders, or functionally graded materials (Long et al., 2013; Obadele et al., 2020; Radhamani et al., 2020; Tokita, 2003; X. Zhang et al., 2021). This study used a spark plasma sintering machine (SPS, FCT Group, Germany) operated under vacuum and a 20 mm graphite die with graphite punches. With this new sintering technique, the tool and the component are directly heated by DC current pulses to reduce cycle times to a few minutes. During SPS a direct pulsed current of 1000 A, voltage of 6V and pulse on/off 15:5 ms was applied. A pyrometer for process temperature regulation was focused on the inside of the top punch of the die. A 0.2 mm thick graphite foil was used to avoid adhesion and reaction between the powders and the graphite mould. Besides this foil, boron nitride spray was applied to reduce carbon diffusion into the sample. For this work, 4 mm high samples were pre-pressed to 10 kN before being set into the SPS machine. The sintering parameters used for the different regolith experiments are given in Table 3, while Table 4 shows the process parameters used to consolidate the metallic powders.

NO.	LUNAR REGOLITH SIMULANT	SINTERING TEMPERATURE (°C)	PRESSURE (MP_A)	HOLDING TIME (min)	MAXIMUM PARTICLE SIZE (µm)
1	LHS-1	900	80	10	200
2	LHS-1	975	80	20	100
3	LHS-1	975	80	20	50
4	LHS-1	1025	80	20	50
5	LHS-1	1050	80	20	50
6	LHS-1	1075	80	20	50
7	LMS-1	1050	80	20	50
8	EAC-1A	1050	80	20	22
9	EAC-1A	1050	80	20	50
10	EAC-1A	1050	80	20	100

TABLE 3 Process parameters used for spark plasma sintering of lunar regolith.

MATERIAL	SINTERING TEMPERATURE (°C)	PRESSURE (MPA)	HOLDING TIME (min)	MAXIMUM PARTICLE SIZE (µm)
Stainless Steel 316L	1050	50	10	30
	1050	50	20	30
	1100	50	20	30
Ti_6Al_4V	1000	50	10	45
	1050	50	10	45

TABLE 4 Process parameters used for spark plasma sintering of metallic powders.

Different experiments were performed to obtain FGM made of EAC-1A and one of the metallic powders: two-step experiments in which metal and lunar regolith were sintered separately under optimal parameters; and a one-step experiment in which both materials were sintered under the same parameters. First, EAC-1A was sintered under the optimal parameters (1050°C, 80 MPa, milled powder), then Ti_6Al_4V was sintered at 1050°C, under 50 MPa with a holding time of 10 min. The optimal process parameters for stainless steel 316L were found to be 1100°C, 50 MPa, and a holding time of 20 min. The steel parameters were similar to those used for full sintering of crushed EAC-1A. The resulting parameters were then applied to another two-step experiment. The first step involved sintering of stainless steel in a layer under optimal parameters, followed by sintering of lunar regolith under its optimal conditions. Second, both layers were sintered under either optimal parameters for lunar regolith or 316L.

Microstructural and morphological characterisation

XRD analysis was performed to determine the phases in the original powders and in the consolidated samples. The analysis was performed with a Bruker D8 Advance diffractometer using Cu K-alpha radiation. The step size used was 0.033° 2θ with 45 kV and 40 mA current in a 2θ range of 10°-100°. The samples were ground with SiC 180 to remove the remaining graphite foil and to enable XRD analysis.

The density of the samples was measured based on Archimedes' principle. The samples were cleaned with isopropanol, dried, and then weighed dry and immersed in distilled water. Three density measurements were taken per sample type and the mean and standard deviation were calculated to give an accuracy range. Spark plasma sintered samples were discs of 20 mm diameter and 4 mm thickness. The specimens were cut into 2 half-discs, then embedded into a conductive resin, ground (SiC 80, 180, 320, 800, 1200 and 2000) and polished (MD Mol 3 µm and MD Nap 1 µm). Optical microscopy (Olympus BX60M) and scanning electron microscopy (SEM) in both secondary and backscattered modes were used for microstructural characterization. Average porosity level and average relative sintered thickness were determined based on optical images. Porosity measurements were taken three times at 5 different locations; accuracy ranges were also taken based on the standard deviation. Energy dispersive spectroscopy (EDS) was performed to determine local composition and elemental distribution in the bulk and interface layers. Thermocalc® calculations were performed to determine the phases formed at the interface of FGM based on EDS results. Microhardness measurements were carried out using an automated Vickers hardness machine, Dura Scan (Struers). A load of 0.3 kgf (HV0.3) was used to measure the hardness of the lunar regolith sintered samples. It was observed that a higher load level results in severe cracking. For the metallic sintered samples, a load of 0.5 kgf (HV0.5) was used to measure their hardness. The hardness was measured at multiple locations on each sample and the average and standard deviation was calculated.

Results and Discussion

Consolidation of lunar regolith

Digital Light Processing (DLP)

Figure 2 shows lunar regolith (EAC-1A) printed samples with a layer thickness of 50 µm. Four bars were successfully printed with a height and width of 5 mm and a length of 100 mm.

The debinding step was successful and the bars remained in their shape after being heat-treated. The colour of the samples after debinding was the same as the initial powder; hence no significant change of the composition of the powder should have occurred. It can thus be concluded that printing and debinding DLP steps can be performed without significant change in chemistry.

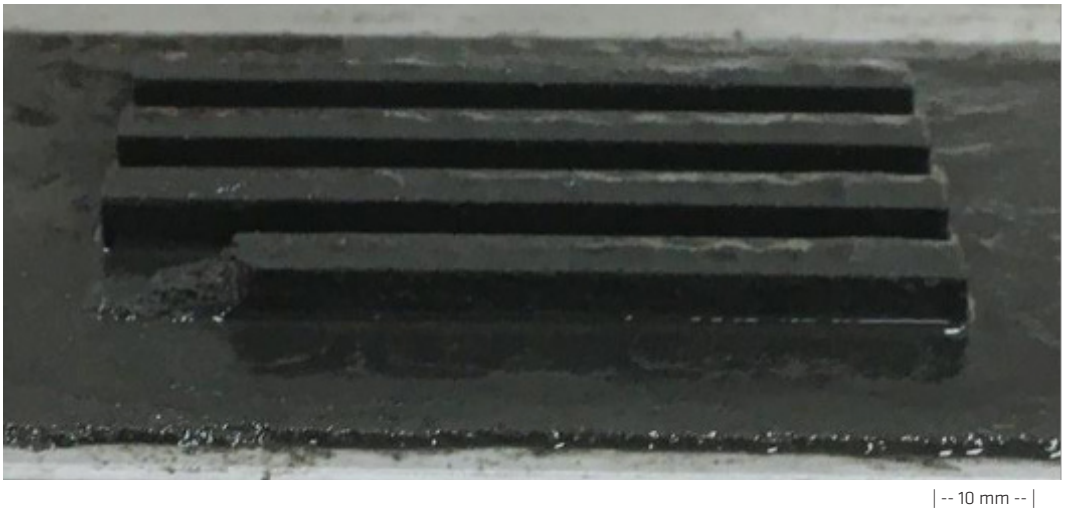

| -- 10 mm -- |

FIGURE 2 DLP printed bars made out of lunar regolith EAC-1A.

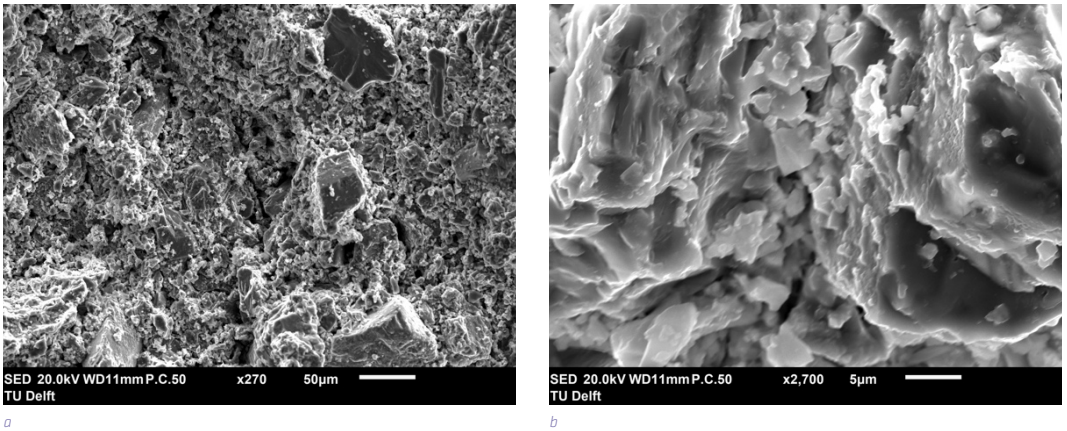

a *b*

FIGURE 3 SEM images of DLP samples sintered under standard in-air conditions: a) low and b) high magnifications.

After standard (in-air) sintering, the samples showed rather poor sintering characteristics: the bars did not keep their shape and cracked into small pieces. The sintered samples also changed in colour, to a light red. A similar colour change was also noticed by Liu et al. (2019), who found it to be associated with the transformation of Fe^{2+} to Fe^{3+} via oxidation reactions. Hence, standard in-air sintering is not suitable for this material and further optimization of the sintering step is required.

The microstructure of the samples showed poor sintering between particles (see Figure 3). However, the structure also shows larger particles surrounded by smaller particles, which would be beneficial for sintering as smaller particles can close the voids between coarser ones, resulting in better packing and densification. Furthermore, as shown in Figure 3b, some particles coalesced and exhibited necking. This partial necking indicates that EAC-1A can be sintered with digital light processing (DLP). However, the sintering process requires further optimization, which is the scope of the follow up sections.

Spark Plasma Sintering (SPS)

SPS is proposed as a follow-up to DLP to increase densification of the lunar regolith. A number of experiments were performed using SPS techniques to optimize the technique. The results were analysed with respect to the sintering temperature, initial powder particle size, and different compositions in the lunar regolith powders.

Effect of SPS temperature

Table 5 shows the effect of SPS temperature on density and hardness. As can be seen, SPS significantly increases the density and hardness while reducing the porosity of lunar regolith simulant samples. The density was found to increase with the sintering temperature, with the maximum density of 2.704 ± 0.025 $g.cm^{-3}$ achieved for the sample sintered at 1075°C. It should be noted that sintering at 1075°C led to partial melting and resulted in a non-stable process. It is therefore advisable to keep the sintering temperature below 1075°C.

SPS TEMPERATURE (°C)	DENSITY (g/cm³)	POROSITY (%)	HARDNESS $HV_{0.3}$
1025	2.532 ± 0.046	23.7 ± 5.4	443 ± 56
1050	2.616 ± 0.060	21.0 ± 5.5	725 ± 77
1075	2.704 ± 0.025	11.7 ± 3.3	743 ± 142

TABLE 5 Density and Vickers hardness of SPS sintered lunar regolith (LHS) samples.

The microstructure of the samples was studied with SEM/EDS and their phases were determined with XRD (Figure 4 and 5). Three main phases were present in the samples at all sintering temperatures: an augite light grey phase $Ca(Mg,Fe,Al)(Si,Al)_2O_6$, a sodian anorthite dark grey phase $(Ca,Na)(Si,Al)_4O_8$ and a white phase corresponding to an iron titanium oxide (Figure 4). The sodian anorthite could have transformed to augite during the SPS experiment. The augite is often found in the form of "smashed" particles within the anorthite phase, as shown in Figure 5. This microstructure could be due to the pressure applied during the SPS process. The partially dissolved anorthite can be pushed between the smashed augite particles by applying external pressure. Anorthite has a lower melting point and a lower modulus than augite: anorthite is thus more prone to plastic deformation under the applied pressure and can fill the gaps between the smashed augite particles (X. Zhang et al., 2019). This specific microstructure was observed for all sintering temperatures.

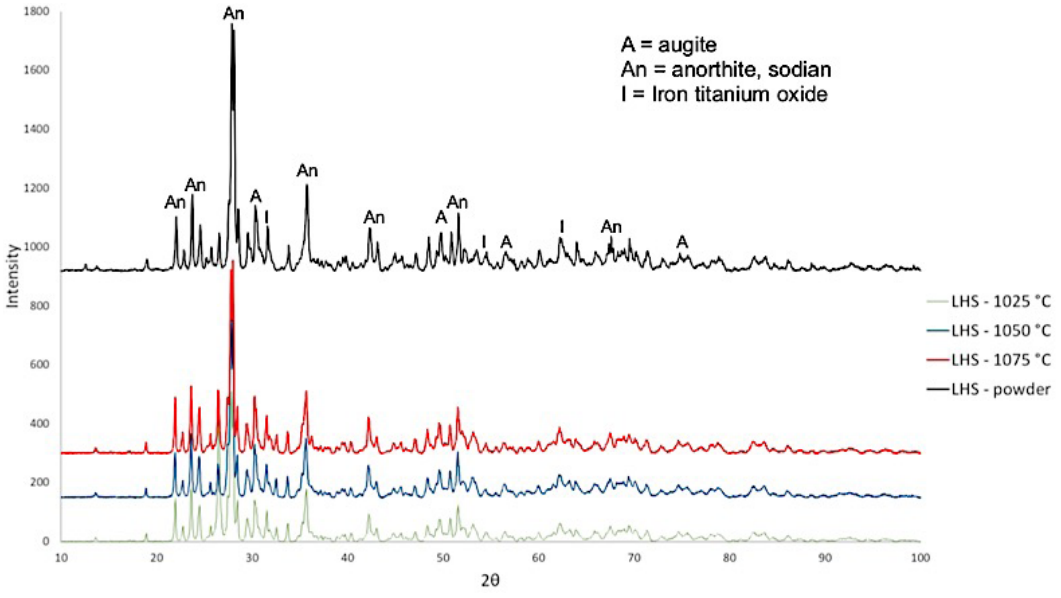

FIGURE 4 XRD patterns of LHS sintered samples as compared to the LHS as-received powder.

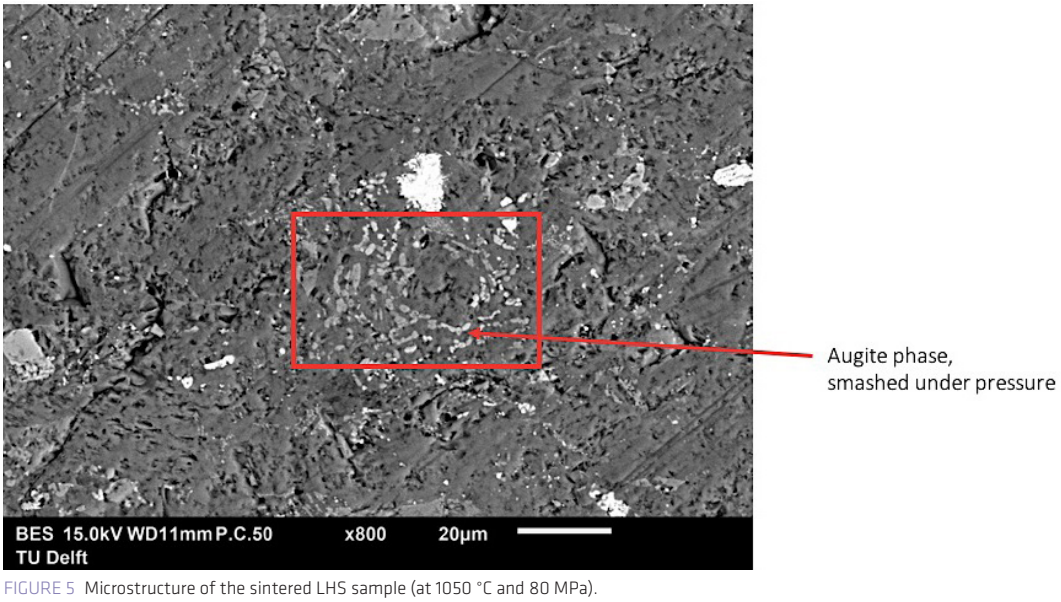

FIGURE 5 Microstructure of the sintered LHS sample (at 1050 °C and 80 MPa).

The XRD patterns for the three different sintering temperatures were very similar: all samples exhibited the same diffraction peaks and were thus composed of the same minerals. This is in accordance with the SEM images, with the same three phases are distinguished: augite, sodian anorthite, and an iron titanium oxide. The compositions of the sintered samples are very similar to the composition of the powder as it was received.

Carbon was detected using EDS only on the outer part of the samples. This carbon originates from the graphite foil used to prevent the powder from sticking to the mould during SPS. Boron nitride was sprayed on the graphite foil to avoid this diffusion, but a small portion of carbon can still diffuse into the samples. Carbon diffusion is a thermally activated process. It increases when using higher sintering temperatures

and higher pressure. Carbon only penetrates over a small layer of the sample and this layer can be removed by mechanical polishing. Viewed using EDS, the carbon was homogeneously present and had not formed any carbides.

Furthermore, the Vickers hardness also increased with the temperature. A significant increase was observed between the sintering temperatures of 1025°C and 1050°C. The hardness measurement is in accordance with the microstructure of the sintered samples. The high standard deviation is related to the different phases present in the specimens and the respective position of the measurement.

Effect of particle size

In order to evaluate the effect of particle size, EAC regolith samples with sieved powders of maximum particle size 22, 50, and 100 µm were sintered at an optimal temperature of 1050°C and 80 MPa.

As can be seen in Table 6, samples with smaller particle size show higher densification. Moreover, the standard deviation is higher for samples with coarser particles, which indicates that the microstructure is more heterogeneous. It should also be noted that more macro-pores were observed in the coarser 100 µm sample. The presence of very coarse particles thus prevents good packing in the powder sample. The sample with the smallest initial particle size is the only sample that showed high vertical densification.

PARTICLE SIZE (µm)	DENSITY (G/CM³)	POROSITY (%)	HARDNESS $HV_{0.3}$
< 22	3.040 ± 0.046	4.3 ± 2.1	722 ± 35
< 50	2.831 ± 0.077	15.5 ± 6.2	752 ± 74
< 100	2.795 ± 0.078	21.4 ± 4.6	657 ± 46

TABLE 6 Density and Vickers hardness of SPS sintered lunar regolith (EAC) samples with different particle size.

The higher densification of samples with finer powders can be related to several densification mechanisms: rearrangement of the particles, formation and growth of the sintering necks between the particles, and plastic deformation and densification (Cheng et al., 2017). The smaller the particle size, the higher the surface energy driving force, given in Equation 1. The powder sintering is enhanced by the higher driving force. This causes migration of particles and increases the contact area between particles.

$$\Delta E = E_p - E_d \approx \gamma_{sv} W_m S_p \quad (1)$$

$$S_p \propto \frac{1}{R} \quad (2)$$

Equations 1 and 2

Equations 1 and 2 show the relationship between the powder properties and the driving force for sintering. ΔE is the intrinsic driving force, E_p is the surface energy of the powder before sintering, E_d the surface energy of powder after sintering, γ_{sv} (J/m²) the solid-gas surface energy, W_m (g/mol) the molar mass of material, S_p (cm²/g) the specific surface area of powder, and R the radius of the particle.

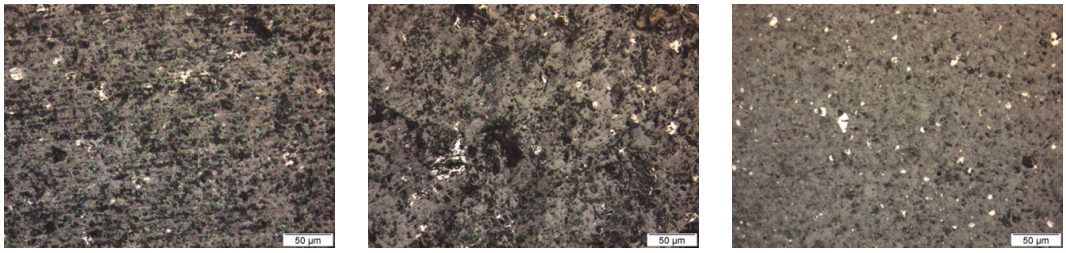

a *b* *c*

FIGURE 6 Optical microscopy images of EAC-1A sintered samples: a) 100 µm, b) 50 µm and c) 22 µm.

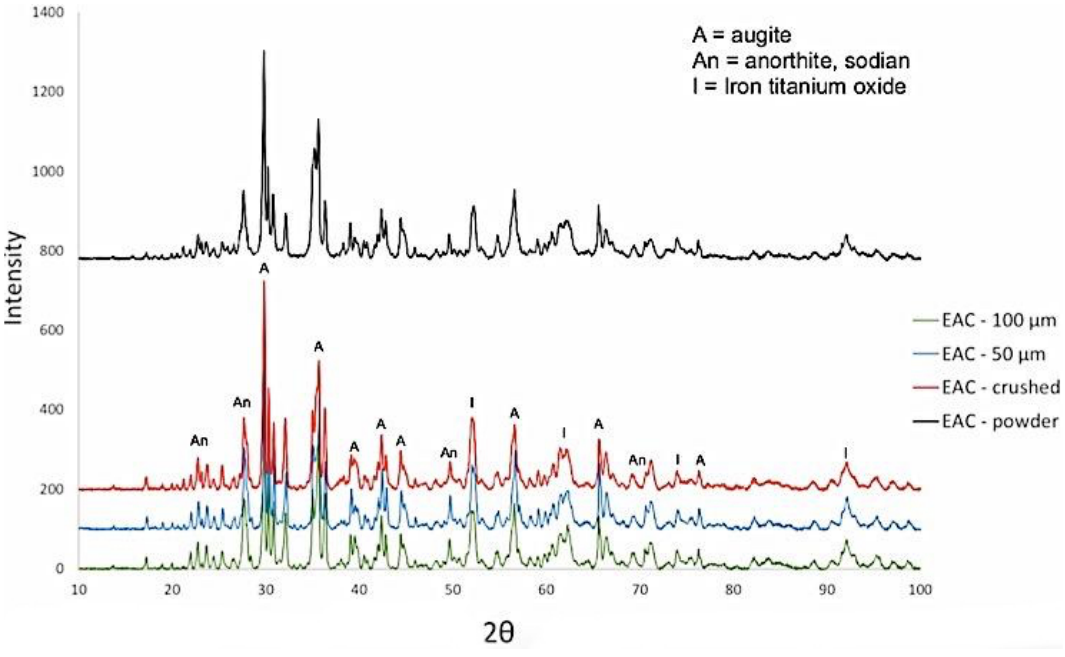

FIGURE 7 XRD patterns for SPS samples with different particle size as compared with as-received powder.

The tensile stress of the sintering necks increases with decreasing particle size, and the strength of the sintering necks is higher between smaller particles. Only the use of crushed EAC-1A powder (with resulting 22 µm particles) led to a fully dense sample (Figure 6c). In the case of SPS, the particle surface is heated to higher temperatures compared to the particle core due to spark discharge in the voids. The surface to volume ratio of smaller particles is bigger than for coarse particles. The amount of the powder subjected to high temperatures is higher in the case of smaller particles, which leads to more effective densification. XRD patterns (Figure 7) showed no significant differences between the samples consolidated with different particle sizes. The primary identified phases were plagioclase, pyroxenes (augite and diopside), and iron titanium oxide. The composition of the sintered samples is close to the composition of the initial powder.

The hardness of the sample with coarse particles is lower than for the other samples. The higher hardness for the sample with maximum particle size 50 µm is associated with a higher standard deviation due to the different hardness of the particles. Thus, the hardness of the 22 µm sample and the 50 µm sample are comparable. The hardness does not increase with powder milling as the phase composition remains similar, yet more homogeneously distributed.

Effect of powder composition

In order to evaluate the effect of regolith simulants and their composition, the LHS-1, EAC-1A, and LMS-1 powders were spark plasma sintered at the previously determined optimal conditions of 1050°C, 80 MPa pressure, and maximum particle size of 50 µm with a holding time of 20 min.

Table 7 shows that all three simulants result in a similar densification level and none of the powders melted under these sintering conditions (1050°C, 80 MPa). The EAC-1A and LMS-1 samples displayed higher densification than the LHS-1 samples. It should however be noted that a thicker layer of fully dense material was measured for the LHS-1 sample. This indicates that the average porosity is lower for LMS-1 and EAC-1A, but LHS-1 has a more heterogeneous porosity with a highly densified part. All three simulants were found to be composed of the same oxides and minerals with comparable phase transition temperatures, and a similar expected behaviour for SPS.

The Vickers hardness of the samples was also not affected by the differences in simulant composition (Table 7). As LMS has more iron titanium oxide phases, the standard deviation could be influenced by these phases' presence at some material locations.

LUNAR REGOLITH SIMULANT TYPE	DENSITY (g/cm^3)	POROSITY (%)	HARDNESS $HV_{0.3}$
LHS-1	2.616 ± 0.060	21.0 ± 5.5	725 ± 77
EAC-1A	2.831 ± 0.077	15.5 ± 6.2	752 ± 74
LMS-1	2.817 ± 0.083	21.6 ± 7.7	732 ± 167

TABLE 7 Density and Vickers hardness of SPS samples of different regolith simulants (max. particle size 50 µm).

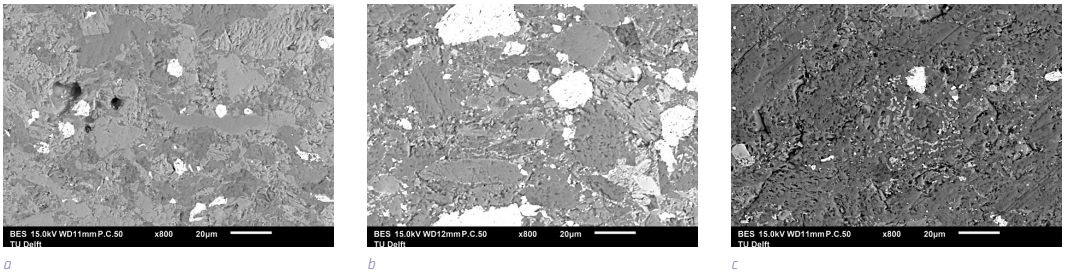

a b c

FIGURE 8 SEM images of SPS samples of three different lunar regolith simulants: a) EAC-1A, b) LMS-1 and c) LHS-1.

The microstructures of the sintered samples were also comparable and dense, with three main phases: augite, sodian anorthite, and iron titanium oxide. The LMS-1 samples showed a higher content of iron titanium oxide and coarser particles than the LHS-1 and EAC-1A samples (see white phases in Figure 8b).

Consolidation of metallic powders

Consolidation of lunar regolith and metallic alloys has to be understood and optimised in order to develop a functionally graded material. The previous sections reviewed the consolidation of lunar regolith and the parameters influencing it. In this section, SPS consolidation of stainless steel and Ti_6Al_4V will be addressed.

Table 8 shows the optimization of SPS parameters based on density and hardness. As can be seen, increasing the sintering temperature increases the density and hardness of stainless steel. The density decrease is relatively low with increased holding time, although other authors observed the opposite trend (Marnier et al., 2014). In our study, the lower density could be due to poor rearrangement of the particles during sintering, preventing the pores from closing. The different balance between open pores and closed pores may also play a role, as the Archimedes measurements only take into account the open pores. However, when porosity is measured using optical techniques, the porosity reduces with increasing temperature.

All Ti_6Al_4V samples showed good densification and almost zero porosity. The applied uniaxial pressure of 50 MPa helps to rearrange the particles, breaking the agglomerates and inducing plastic deformation at high temperatures. The Joule heating effect derived from the pulsed current is another important densification mechanism. The current can flow through the highly conductive powdered sample, heating up the particles, especially on the particle surfaces. The temperature is thus higher at the contact point between particles. Diffusion thus increases and leads to higher and easier densification (Crosby et al., 2014).

Table 8 shows that the hardness for both alloys increased with rising sintering temperature. The hardness of samples sintered at 1050°C is in the order of the hardness of the cast annealed 316 alloys. The samples sintered at 1100°C show a much higher hardness. The hardness was homogeneous across the whole sample and the standard deviation is relatively small for all samples, indicating that the microstructure and composition are also likely homogeneous. SEM analysis revealed a homogeneous microstructure for all samples and did not show any precipitates. Some nano-precipitates could be present, such as carbides due to carbon diffusion. However, they are not visible at the magnification used. Some authors reported the presence of carbides on grain boundaries (Marnier et al., 2014). Nevertheless, these carbides were found only on the thin edges of the samples.

MATERIAL	TEMPERATURE / HOLDING TIME	DENSITY (g/cm³)	POROSITY (%)	HARDNESS $HV_{0.5}$
Stainless Steel 316	1050 °C/10 min	7.642 ± 0.046	3 ± 1.2	158 ± 5
	1050 °C/20 min	7.556 ± 0.015	1.4 ± 0.4	164 ± 6
	1100 °C/20 min	7.834 ± 0.010	0.9 ± 0.3	191 ± 5
Ti_6Al_4V	1000 °C/10 min	4.391 ± 0.018	1.2 ± 0.5	322 ± 11
	1050 °C/10 min	4.389 ± 0.006	0.7 ± 0.2	341 ± 23

TABLE 8 Density and Vickers hardness of sintered stainless steel and Ti_6Al_4V (under 50 MPa pressure).

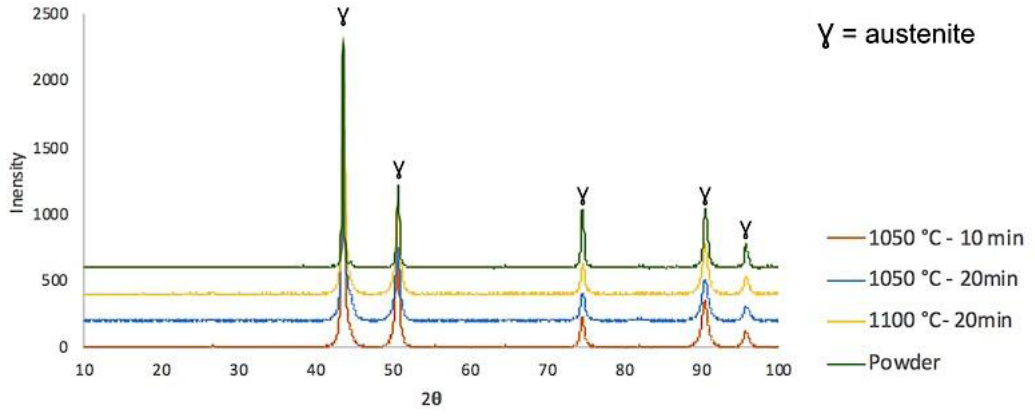

FIGURE 9 XRD of SPSed stainless steel 316 samples and of as-received powder.

The Vickers hardness for Ti_6Al_4V was found to be 341 $HV_{0.5}$ for the samples sintered at 1050°C, compared to 322 $HV_{0.5}$ for the sample sintered at 1000 °C. These values are in the order of the Vickers hardness for Ti_6Al_4V cast alloys (Poondla et al., 2009).

The XRD results in Figure 9 reveal only austenite phases present in all 316L samples. This fully austenitic microstructure was also observed by Keller et al. (2016).

For Ti_6Al_4V alloys, the elements Ti, Al, and V were found to be evenly distributed, and no precipitates formed during the sintering process. The XRD results in Figure 10 show that the same phases form at the two different sintering temperatures. The α-Ti phase is present as in the as-received powder, but a second phase is detected for both samples: $Ti_{0.8}V_{0.2}$, which is a β-Ti structure.

Microstructural analysis revealed the presence of clusters of grains elongated in the same direction. Recrystallization is not hindered by the presence of intermetallics at the grain boundaries or by interstitial solute atoms, as shown by Long et al. (2013).

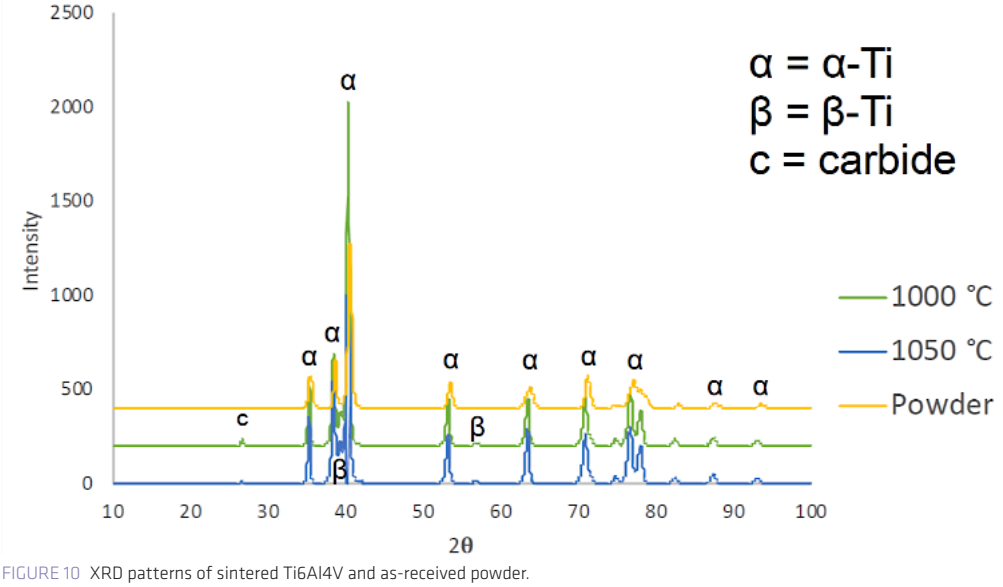

FIGURE 10 XRD patterns of sintered Ti6Al4V and as-received powder.

Consolidation of functionally graded material (FGM)

The optimized parameters for FGM samples are based on the sintering results from regolith simulant and the individual metallic powders. The optimal SPS parameters for each material are displayed in Table 9.

MATERIAL	SINTERING TEMPERATURE (°C)	PRESSURE (MPA)	HOLDING TIME (MIN)	MAXIMUM PARTICLE SIZE (MM)
Lunar regolith simulant EAC-1A	1050	80	20	22
Stainless steel 316L	1100	50	20	30
Ti6Al4V	1050	50	10	45

TABLE 9 Optimal parameters for SPS of FGM based on lunar regolith simulant, stainless steel and titanium alloy.

3.3.1. FGM based on lunar regolith and stainless steel

The sintering was initially performed in one step by combining both lunar regolith (EAC-1A) and 316L green bodies. The experiment resulted in an inconsistent FGM and interfacial cracking. The one-step sintering at 1100°C under 50 MPa completely melted the lunar regolith simulant, which was squeezed out of the SPS mould. The surface of the metallic part did not show any remnants of the lunar regolith. This experiment highlights that sintering at 1100°C under 50 MPa is not suitable for the FGM lunar regolith simulant.
When sintering both powders at 1050°C under 50 MPa, the FGM did not keep its shape and the EAC-1A and stainless-steel layers did not bond. Both layers exhibited cracks and porosity at the FGM interface, see Figure 11. Thus, pressure of 50 MPa proved too low to allow for good sintering of the two powders.
A minimal pressure of 80 MPa seemed to be required to sinter the lunar regolith, and a higher pressure may be required to allow for interfacial sintering.
Therefore, a two-step sintering was introduced and proved to be more successful. The thin layer of EAC-1A remained in contact with the metal. However, the FGM fractured within the lunar regolith layer upon removal from the SPS mould. This might be caused by the thermal expansion coefficient of stainless steel 316, which is twice as high as the lunar regolith (Ray et al., 2010). This mismatch in thermal properties induces thermal stresses during SPS cooling. These stresses can explain why the FGMs cracked post-sintering.
However, the interface between the two dissimilar materials remained intact. SEM images revealed the presence of a grey phase at the interface, featuring higher chromium concentration than in the inner layers (Figure 13a). Chromium tends to diffuse from the stainless steel to the interface and form a high-content Cr phase; according to Thermocalc® calculations and composition from EDS, this is likely to be a BCC-A2 phase (Figure 12). Figure 13 shows the 316L/EAC functionally graded material hardness profile. The interface has a hardness much closer to the metallic alloy and does not exhibit a gradual transition, which is preferred for FGMs. Each hardness value was averaged based on 10 measurements for each location. Since the change in hardness between the interface and the lunar regolith is relatively large, it could explain the poor sintering properties of this type of FGM.

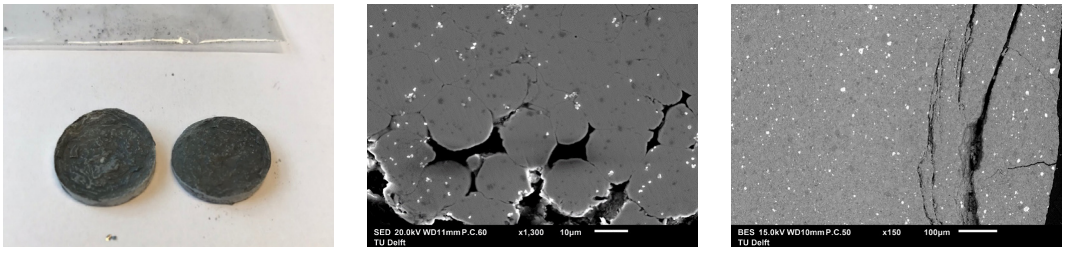

a b c

FIGURE 11 a) FGM 316/EAC after sintering at 1050°C. SEM images of the interface between the two materials: b) SS 316L and c) EAC-1A.

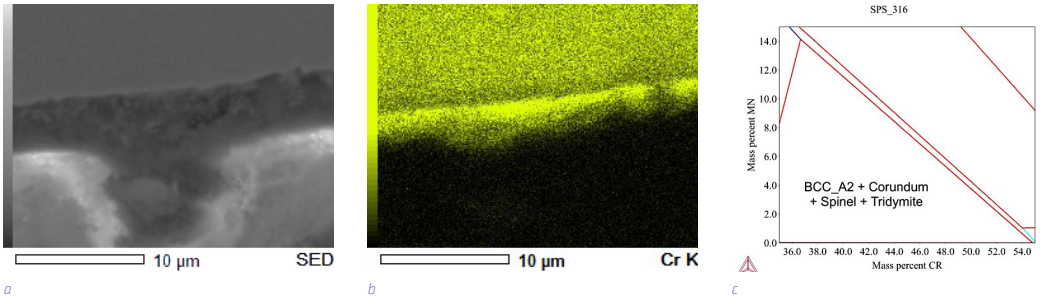

a b c

FIGURE 12 a) SEM image of interface of FGM 316/EAC, b) EDS map of Cr at the interface of FGM 316/EAC and c) Thermocalc graph for Cr diffusion.

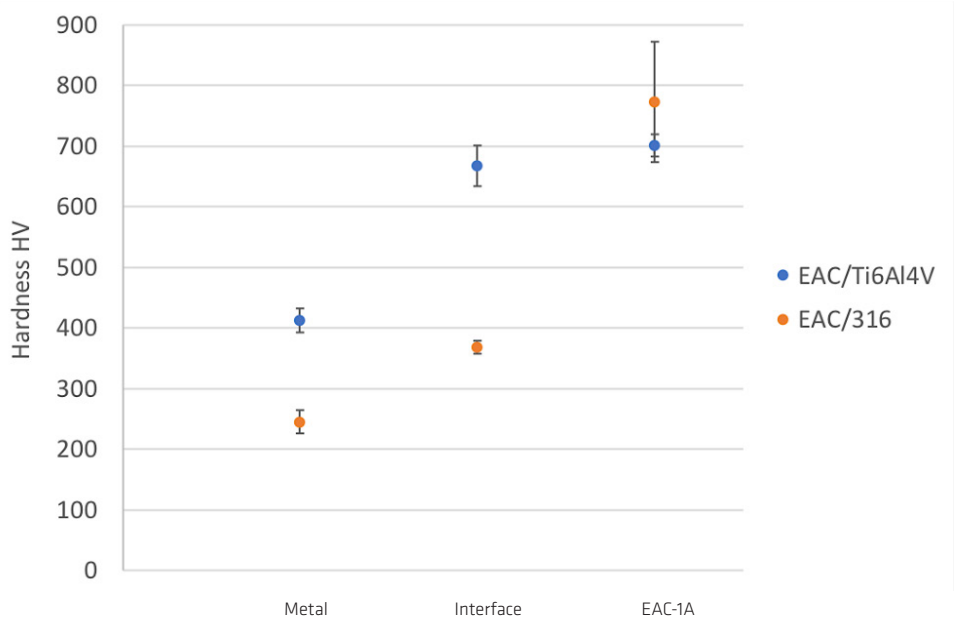

FIGURE 13 Vickers hardness profile of the functionally graded materials.

3.3.2. FGM based on lunar regolith and Ti_6Al_4V alloy

Ti_6Al_4V is the second alloy, selected for its good compatibility with lunar regolith. The FGM samples (Figure 14) produced did not show any fractures, cracking, or interfacial porosity, which were characteristic of the previous 316L/EAC FGM. As shown in Figure 13b, white particles, identified as titanium oxide, are present at the interface between the lunar regolith and Ti_6Al_4V. Moreover, EDS measurements reveal a potential segregation of silicon at the interface (Figure 15b), which forms the phase HCP_A3 (Ti_xSi_y) according to Thermocalc® calculations (Figure 15c).

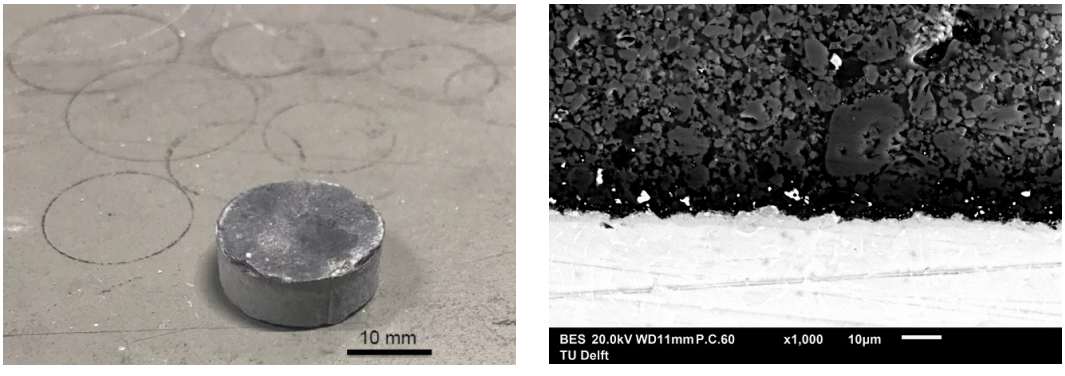

a *b*

FIGURE 14 a) FGM Ti_6Al_4V/EAC-1A after sintering in 2 steps and b) SEM image of the interface between Ti_6Al_4V (light, below) and EAC-1A (dark, above).

The Vickers hardness profile of this FGM shows a gradual transition from one material to another at interface (Figure 13). The hardness of the interface is close to the hardness of the lunar regolith. The coefficient of thermal expansion of Ti_6Al_4V and lunar regolith simulant are very close, about $8x10^{-6}$ K^{-1} for both materials (Karami et al., 2020; Ray et al., 2010; Yakout et al., 2020). The similar coefficients help to prevent high thermal stresses during sintering, and especially during the cooling stage.

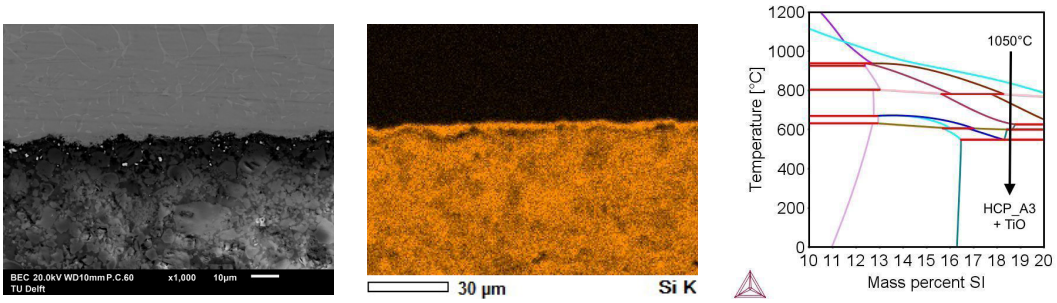

a b c

FIGURE 15 a) SEM image of interface of FGM Ti6Al4V/EAC, b) EDS of Si at the interface of FGM and Ti6Al4V c) Thermocalc graph for Ti6Al4V/EAC interface.

Conclusions

In-situ resource utilization and advanced materials are essential for future space habitation on the Moon. In this study, additive manufacturing and spark plasma sintering were used to investigate the feasibility of a functional graded metallic-regolith. First, lunar regolith simulants were printed and debinded using digital light processing. Second, spark plasma sintering was applied and optimized using different sintering conditions, namely temperature, particle size, and composition. Then, the same SPS approach was applied to the metallic powders. Finally, the optimal processing conditions were developed for consolidation of functionally graded metallic-regolith with respect to densification, microstructural, compositional, and microhardness characteristics. The following conclusions are drawn from this study:

Lunar regolith simulants can be successfully additively manufactured via a combination of digital light processing and spark plasma sintering at 1050°C under 80 MPa. For best densification, it is necessary to sieve or mill the powders to 20-50 µm range. A higher pressure could be used to avoid the milling step. The composition of the sintered samples is similar to the powder composition: mainly augite, sodian anorthite, and iron titanium oxide.

Increasing the temperature and reducing the particle size in this process was found to increase densification and Vickers micro-hardness.

Metallic powders can be fully densified with SPS at relatively low temperature and a pressure of 50 MPa. Both stainless steel and Ti_6Al_4V showed a homogeneous structure without precipitates or carbides.

FGMs were made using the optimal SPS parameters. The combination of lunar regolith and Ti_6Al_4V has proven to be the most promising gradient. The hardness profile showed a gradual transition between these two layers, while the interface was found to be strong enough to avoid cracking.

This FGM feasibility study showed promising results for using additive manufacturing and in-space resources. The authors recommend the following aspects for follow-up research:

Investigations of the mechanical properties of regolith-metallic FGMs are needed, in particular of compressive strength, fracture toughness, and thermal fatigue behaviour for lunar construction applications, and wear resistance for coating applications. Thermal and wear properties are thought likely to be improved over metallic substrate alone, whereby fracture resistance will be greater than regolith alone. Understanding these properties is a major next step toward validating this method for lunar applications.

The combination of regolith with other metals in pure composition, such as pure aluminium, iron, and titanium powders, is needed to determine optimal FGM manufacturing in conditions closer to a lunar scenario.

In order to adapt the DLP method for lunar infrastructure, the next step is to investigate compatible resins. Furthermore, the debinding step should be optimised for the lunar environment to prevent charcoal formation and defects by tailoring powder morphology, resin, heating rate, and geometry.

Moreover, the SPS technique would have to be modified to be employed on the Moon for large-scale production. This study showed local melting of the powder at 1075 °C. Thus, laser-based additive manufacturing techniques could be investigated as a method for applying lunar regolith as a coating onto metallic surfaces to achieve better wear, corrosion, and thermal resistance.

The DLP process holds a uniquely high potential for printing complex geometries. Further studies could investigate methods for high-pressure sintering of complex green bodies in order to make full use of the DLP potential for FGM manufacture.

Acknowledgments

The authors would like to acknowledge the support of the European Space Agency (ESA) via the Ariadna 19-D-A-02 research funding. Furthermore, we would like to express gratitude to the ESA technicians at the European Space Research and Technology Centre (ESTEC), in particular to Advenit Makaya, Sarah Rodríguez Castillo, and Martina Meisnar, as well as Jaap Hooijmans at Admatec for his assistance in performing DLP.

References

AGOSTO, W. (1981, May). BENEFICIATION AND POWDER METALLURGICAL PROCESSING OF LUNAR SOIL METAL. *4th Space Manufacturing; Proceedings of the Fifth Conference*. https://doi.org/10.2514/6.1981-3263

Allen, C. C., Morris, R. V., & McKay, D. S. (1996). Oxygen extraction from lunar soils and pyroclastic glass. *Journal of Geophysical Research: Planets*, *101*(E11), 26085–26095. https://doi.org/10.1029/96je02726

Altun, A. A., Ertl, F., Marechal, M., Makaya, A., Sgambati, A., & Schwentenwein, M. (2021). Additive manufacturing of lunar regolith structures. *Open Ceramics*, *5*, 100058. https://doi.org/10.1016/j.oceram.2021.100058

Balla, V. K., Bandyopadhyay, P. P., Bose, S., & Bandyopadhyay, A. (2007). Compositionally graded yttria-stabilized zirconia coating on stainless steel using laser engineered net shaping (LENSTM). *Scripta Materialia*, *57*(9), 861–864. https://doi.org/10.1016/j.scriptamat.2007.06.055

Balla, V. K., Roberson, L. B., O'Connor, G. W., Trigwell, S., Bose, S., & Bandyopadhyay, A. (2012). First demonstration on direct laser fabrication of lunar regolith parts. *Rapid Prototyping Journal*, *18*(6), 451–457. https://doi.org/10.1108/13552541211271992

Benaroya, H. (2018). *Building Habitats on the Moon: Engineering Approaches to Lunar Settlements (Springer Praxis Books)* (1st ed.). Springer.

Bever, M., & Duwez, P. (1972). Gradients in composite materials. *Materials Science and Engineering*, *10*, 1–8. https://doi.org/10.1016/0025-5416(72)90059-6

Brown, G. M., Peckett, A., Emeleus, C. H., Phillips, R., & Pinsent, R. H. (1975). *Petrology and mineralogy of Apollo 17 mare basalts*. 1–13.

Cannon, K. (n.d.-a). *LHS-1 Lunar Highlands Simulant*. Planetary Simulant Database. Retrieved November 25, 2020, from https://simulantdb.com/simulants/lhs1.php

Cannon, K. (n.d.-b). *LMS-1 Lunar Mare Simulant*. Planetary Simulant Database. Retrieved November 25, 2020, from https://simulantdb.com/simulants/lms1.php

Cesaretti, G., Dini, E., De Kestelier, X., Colla, V., & Pambaguian, L. (2014). Building components for an outpost on the Lunar soil by means of a novel 3D printing technology. *Acta Astronautica*, *93*, 430–450. https://doi.org/10.1016/j.actaastro.2013.07.034

Cheibas, I., Laot, M., Popovich, V. A., Rich, B., & Castillo, S. R. (2020). *Additive Manufacturing of Functionally Graded Materials with In-Situ Resources*. Aerospace Europe Conference, Bordeaux, France.

Cheng, Y., Cui, Z., Cheng, L., Gong, D., & Wang, W. (2017). Effect of particle size on densification of pure magnesium during spark plasma sintering. *Advanced Powder Technology*, *28*(4), 1129–1135. https://doi.org/10.1016/j.apt.2017.01.017

Chua, C. K., Wong, C. H., & Yeong, W. Y. (2017). *Standards, Quality Control, and Measurement Sciences in 3D Printing and Additive Manufacturing*. Academic Press.

CLASS Exolith Lab. (n.d.-a). Center for Lunar & Asteroid Surface Science. Retrieved November 6, 2020, from https://sciences.ucf.edu/class/exolithlab/

CLASS Exolith Lab. (n.d.-b). *LHS-1 Lunar Highlands Simulant Fact Sheet*. Exolith Lab. Retrieved November 6, 2020, from https://exolithsimulants.com/collections/regolith-simulants/products/lhs-1-lunar-highlands-simulant

CLASS Exolith Lab. (n.d.-c). *LMS-1 Lunar Mare Simulant Fact Sheet*. Exolith Lab. Retrieved November 6, 2020, from https://exolithsimulants.com/collections/regolith-simulants/products/lms-1-lunar-mare-simulant

Crosby, K., Shaw, L. L., Estournes, C., Chevallier, G., Fliflet, A. W., & Imam, M. A. (2014). Enhancement in Ti–6Al–4V sintering via nanostructured powder and spark plasma sintering. *Powder Metallurgy*, *57*(2), 147–154. https://doi.org/10.1179/1743290113y.0000000082

Dordlofva, C., & Törlind, P. (Eds.). (2017). *Qualification Challenges with Additive Manufacturing in Space Applications*. .

Eckart, P. (1999). *The Lunar Base Handbook (Space Technology Series)* (1st ed.). McGraw-Hill Primis Custom Publishing.

Edmunson, J., & Rickman, D. L. (2012). A Survey of Geologic Resources. In V. Badescu (Ed.), *Moon* (pp. 1–21). Springer. https://doi.org/10.1007/978-3-642-27969-0_1

Engelschiøn, V. S., Eriksson, S. R., Cowley, A., Fateri, M., Meurisse, A., Kueppers, U., & Sperl, M. (2020). EAC-1A: A novel large-volume lunar regolith simulant. *Scientific Reports*, *10*(1). https://doi.org/10.1038/s41598-020-62312-4

F42 Committee. (n.d.). *Terminology for Additive Manufacturing Technologies*. ASTM International. https://doi.org/10.1520/F2792-12A

Fateri, M., Meurisse, A., Sperl, M., Urbina, D., Madakashira, H. K., Govindaraj, S., Gancet, J., Imhof, B., Hoheneder, W., Waclavicek, R., Preisinger, C., Podreka, E., Mohamed, M. P., & Weiss, P. (2019). Solar Sintering for Lunar Additive Manufacturing. *Journal of Aerospace Engineering*, *32*(6), 04019101. https://doi.org/10.1061/(asce)as.1943-5525.0001093

Fateri, M., Pitikaris, S., & Sperl, M. (2019). Investigation on Wetting and Melting Behavior of Lunar Regolith Simulant for Additive Manufacturing Application. *Microgravity Science and Technology*, *31*(2), 161–167. https://doi.org/10.1007/s12217-019-9674-5

Frank, J., Spirkovska, L., McCann, R., Lui Wang, Pohlkamp, K., & Morin, L. (2013). Autonomous mission operations. *2013 IEEE Aerospace Conference*, 1–20. https://doi.org/10.1109/aero.2013.6496927

Gong, F., Zhao, J., Li, Z., Sun, J., Ni, X., & Hou, G. (2018). Design, fabrication and mechanical properties of multidimensional graded ceramic tool materials. *Ceramics International*, *44*(3), 2941–2951. https://doi.org/10.1016/j.ceramint.2017.11.046

Goulas, A., Binner, J. G., Engstrøm, D. S., Harris, R. A., & Friel, R. J. (2018). Mechanical behaviour of additively manufactured lunar regolith simulant components. *Proceedings of the Institution of Mechanical Engineers, Part L: Journal of Materials: Design and Applications*, *233*(8), 1629–1644. https://doi.org/10.1177/1464420718777932

Goulas, A., Binner, J. G., Harris, R. A., & Friel, R. J. (2017). Assessing extraterrestrial regolith material simulants for in-situ resource utilisation based 3D printing. *Applied Materials Today*, *6*, 54–61. https://doi.org/10.1016/j.apmt.2016.11.004

Goulas, A., & Friel, R. J. (2016). 3D printing with moondust. *Rapid Prototyping Journal*, *22*(6), 864–870. https://doi.org/10.1108/rpj-02-2015-0022

Howe, A. S., & Sherwood, B. (2009). *Out of this world: The new field of space architecture*. American Institute of Aeronautics & Astronautics.

Jin, Q., Ren, X. P., Hou, H. L., Zhang, Y. L., & Qu, H. T. (2018). In Situ Synthesis and Structural Design of Ti/TiC Functionally Graded Materials. *Materials Science Forum*, *913*, 515–521. https://doi.org/10.4028/www.scientific.net/msf.913.515

Kamaruzaman, F. F., Nuruzzaman, D. M., Ismail, N. M., Hamedon, Z., Iqbal, A. K. M. A., & Azhari, A. (2018). Microstructure and properties of aluminium-aluminium oxide graded composite materials. *IOP Conference Series: Materials Science and Engineering*, *319*, 012046. https://doi.org/10.1088/1757-899x/319/1/012046

Karami, K., Blok, A., Weber, L., Ahmadi, S. M., Petrov, R., Nikolic, K., Borisov, E. V., Leeflang, S., Ayas, C., Zadpoor, A. A., Mehdipour, M., Reinton, E., & Popovich, V. A. (2020). Continuous and pulsed selective laser melting of Ti_6Al_4V lattice structures: Effect of post-processing on microstructural anisotropy and fatigue behaviour. *Additive Manufacturing*, *36*, 101433. https://doi.org/10.1016/j.addma.2020.101433

Katz-Demyanetz, A., Popov, V. V., Kovalevsky, A., Safranchik, D., & Koptyug, A. (2019). Powder-bed additive manufacturing for aerospace application: Techniques, metallic and metal/ceramic composite materials and trends. *Manufacturing Review*, *6*, 5. https://doi.org/10.1051/mfreview/2019003

Keller, C., Tabalaiev, K., Marnier, G., Noudem, J., Sauvage, X., & Hug, E. (2016). Influence of spark plasma sintering conditions on the sintering and functional properties of an ultra-fine grained 316L stainless steel obtained from ball-milled powder. *Materials Science and Engineering: A*, *665*, 125–134. https://doi.org/10.1016/j.msea.2016.04.039

Kennedy, K. (2002). The Vernacular of Space Architecture. *AIAA Space Architecture Symposium*. https://doi.org/10.2514/6.2002-6102

Khoshnevis, B., Bodiford, M., Burks, K., Ethridge, E., Tucker, D., Kim, W., Toutanji, H., & Fiske, M. (2005). Lunar Contour Crafting - A Novel Technique for ISRU-Based Habitat Development. *43rd AIAA Aerospace Sciences Meeting and Exhibit*. https://doi.org/10.2514/6.2005-538

Kim, B.-H., & Na, Y.-H. (1995). Fabrication of fiber-reinforced porous ceramics of Al2O3-mullite and SiC-mullite systems. *Ceramics International*, *21*(6), 381–384. https://doi.org/10.1016/0272-8842(95)94461-i

Labeaga-Martínez, N., Sanjurjo-Rivo, M., Díaz-Álvarez, J., & Martínez-Frías, J. (2017). Additive manufacturing for a Moon village. *Procedia Manufacturing*, *13*, 794–801. https://doi.org/10.1016/j.promfg.2017.09.186

Landis, G. A. (2007). Materials refining on the Moon. *Acta Astronautica*, *60*(10–11), 906–915. https://doi.org/10.1016/j.actaastro.2006.11.004

Liu, M., Tang, W., Duan, W., Li, S., Dou, R., Wang, G., Liu, B., & Wang, L. (2019). Digital light processing of lunar regolith structures with high mechanical properties. *Ceramics International*, *45*(5), 5829–5836. https://doi.org/10.1016/j.ceramint.2018.12.049

Long, Y., Zhang, H., Wang, T., Huang, X., Li, Y., Wu, J., & Chen, H. (2013). High-strength Ti–6Al–4V with ultrafine-grained structure fabricated by high energy ball milling and spark plasma sintering. *Materials Science and Engineering: A*, *585*, 408–414. https://doi.org/10.1016/j.msea.2013.07.078

Manick, K., Gill, S.-J., Rumsey, M. S., Smith, C. L., Duvet, L., Miller, C. G., & Jones, C. (2018, March). *The European Space Agency Exploration Sample Analogue Collection (Esa2c) And Curation Facility – Present And Future* [Paper presentation]. 49th Lunar and Planetary Science Conference, The Woodlands, Texas.

Marnier, G., Keller, C., Noudem, J., & Hug, E. (2014). Functional properties of a spark plasma sintered ultrafine-grained 316L steel. *Materials & Design*, *63*, 633–640. https://doi.org/10.1016/j.matdes.2014.06.053

Maseko, S. W., Popoola, A. P. I., & Fayomi, O. S. I. (2018). Characterization of ceramic reinforced titanium matrix composites fabricated by spark plasma sintering for anti-ballistic applications. *Defence Technology*, *14*(5), 408–411. https://doi.org/10.1016/j.dt.2018.04.013

Mertens, A. I., Reginster, S., Paydas, H., Contrepois, Q., Dormal, T., Lemaire, O., & Lecomte-Beckers, J. (2014). Mechanical properties of alloy Ti–6Al–4V and of stainless steel 316L processed by selective laser melting: influence of out-of-equilibrium microstructures. *Powder Metallurgy*, *57*(3), 184–189. https://doi.org/10.1179/1743290114y.0000000092

Meurisse, A., Beltzung, J. C., Kolbe, M., Cowley, A., & Sperl, M. (2017). Influence of Mineral Composition on Sintering Lunar Regolith. *Journal of Aerospace Engineering*, *30*(4), 04017014. https://doi.org/10.1061/(asce)as.1943-5525.0000721

Meurisse, A., Makaya, A., Willsch, C., & Sperl, M. (2018). Solar 3D printing of lunar regolith. *Acta Astronautica*, *152*, 800–810. https://doi.org/10.1016/j.actaastro.2018.06.063

Mueller, S., Taylor, G. J., & Phillips, R. J. (1988). Lunar composition: A geophysical and petrological synthesis. *Journal of Geophysical Research*, *93*(B6). https://doi.org/10.1029/jb093ib06p06338

Munir, Z. A., Anselmi-Tamburini, U., & Ohyanagi, M. (2006). The effect of electric field and pressure on the synthesis and consolidation of materials: A review of the spark plasma sintering method. *Journal of Materials Science*, *41*(3), 763–777. https://doi.org/10.1007/s10853-006-6555-2

Naser, M. Z., & Chehab, A. I. (2018). Materials and design concepts for space-resilient structures. *Progress in Aerospace Sciences*, *98*, 74–90. https://doi.org/10.1016/j.paerosci.2018.03.004

Neves, J. M., Ramanathan, S., Suraneni, P., Grugel, R., & Radlińska, A. (2020). Characterization, mechanical properties, and microstructural development of lunar regolith simulant-portland cement blended mixtures. *Construction and Building Materials*, *258*, 120315. https://doi.org/10.1016/j.conbuildmat.2020.120315

Obadele, B. A., Adesina, O. S., Oladijo, O. P., & Ogunmuyiwa, E. N. (2020). Fabrication of functionally graded 316L austenitic and 2205 duplex stainless steels by spark plasma sintering. *Journal of Alloys and Compounds*, *849*, 156697. https://doi.org/10.1016/j.jallcom.2020.156697

Papike, J. J., Simon, S. B., & Laul, J. C. (1982). The lunar regolith: Chemistry, mineralogy, and petrology. *Reviews of Geophysics*, *20*(4), 761. https://doi.org/10.1029/rg020i004p00761

Pieters, C. M. (1986). Composition of the lunar highland crust from near-infrared spectroscopy. *Reviews of Geophysics*, *24*(3). https://doi.org/10.1029/rg024i003p00557

Pilehvar, S., Arnhof, M., Pamies, R., Valentini, L., & Kjøniksen, A. L. (2020). Utilization of urea as an accessible superplasticizer on the moon for lunar geopolymer mixtures. *Journal of Cleaner Production*, *247*, 119177. https://doi.org/10.1016/j.jclepro.2019.119177

Poondla, N., Srivatsan, T. S., Patnaik, A., & Petraroli, M. (2009). A study of the microstructure and hardness of two titanium alloys: Commercially pure and Ti–6Al–4V. *Journal of Alloys and Compounds*, *486*(1–2), 162–167. https://doi.org/10.1016/j.jallcom.2009.06.172

Popovich, V. A., Borisov, E. V., Heurtebise, V., Riemslag, T., Popovich, A. A., & Sufiiarov, V. S. (2018). Creep and Thermomechanical Fatigue of Functionally Graded Inconel 718 Produced by Additive Manufacturing. *TMS 2018 147th Annual Meeting & Exhibition Supplemental Proceedings*, 85–97. https://doi.org/10.1007/978-3-319-72526-0_9

Prettyman, T. H., Hagerty, J. J., Elphic, R. C., Feldman, W. C., Lawrence, D. J., McKinney, G. W., & Vaniman, D. T. (2006). Elemental composition of the lunar surface: Analysis of gamma ray spectroscopy data from Lunar Prospector. *Journal of Geophysical Research: Planets*, *111*(E12). https://doi.org/10.1029/2005je002656

Radhamani, A. V., Lau, H. C., Kamaraj, M., & Ramakrishna, S. (2020). Structural, mechanical and tribological investigations of CNT-316 stainless steel nanocomposites processed via spark plasma sintering. *Tribology International*, *152*, 106524. https://doi.org/10.1016/j.triboint.2020.106524

Rajan, T. P. D., & Pai, B. C. (2014). Developments in Processing of Functionally Gradient Metals and Metal–Ceramic Composites: A Review. *Acta Metallurgica Sinica (English Letters)*, *27*(5), 825–838. https://doi.org/10.1007/s40195-014-0142-3

Rattanachan, S., Miyashita, Y., & Mutoh, Y. (2003). Microstructure and fracture toughness of a spark plasma sintered Al2O3-based composite with BaTiO3 particulates. *Journal of the European Ceramic Society*, *23*(8), 1269–1276. https://doi.org/10.1016/s0955-2219(02)00294-7

Ray, C. S., Reis, S. T., Sen, S., & O'Dell, J. S. (2010). JSC-1A lunar soil simulant: Characterization, glass formation, and selected glass properties. *Journal of Non-Crystalline Solids*, *356*(44–49), 2369–2374. https://doi.org/10.1016/j.jnoncrysol.2010.04.049

Restivo, T. A. G., Beccari, R. F., Padilha, W. R., Durazzo, M., Telles, V. B., Coleti, J., Yamagata, C., Silva, A. C. D., Suzuki, E., Soares Tenório, J. A. S., & Mello-Castanho, S. R. H. (2019). Micrograded ceramic-metal composites. *Journal of the European Ceramic Society*, *39*(12), 3484–3490. https://doi.org/10.1016/j.jeurceramsoc.2019.03.018

Ruys, A. J., Popov, E. B., Sun, D., Russell, J. J., & Murray, C. C. J. (2001). Functionally graded electrical/thermal ceramic systems. *Journal of the European Ceramic Society*, *21*(10–11), 2025–2029. https://doi.org/10.1016/s0955-2219(01)00165-0

Sanders, G. B., Romig, K. A., Larson, W. E., Johnson, R., Rapp, D., Johnson, K. R., Sacksteder, K., Linne, D., Curreri, P., Duke, M., Blair, B., Gertsch, L., Boucher, D., Rice, E., Clark, L., McCullough, E., & Zubrin, R. (2005). *Results from the NASA Capability Roadmap Team for In-Situ Resource Utilization (ISRU)*. International Lunar Conference.

Schleppi, J., Gibbons, J., Groetsch, A., Buckman, J., Cowley, A., & Bennett, N. (2018). Manufacture of glass and mirrors from lunar regolith simulant. *Journal of Materials Science*, *54*(5), 3726–3747. https://doi.org/10.1007/s10853-018-3101-y

Shiwei, N., Dritsas, S., & Fernandez, J. G. (2020). Martian biolith: A bioinspired regolith composite for closed-loop extraterrestrial manufacturing. *PLOS ONE*, *15*(9), e0238606. https://doi.org/10.1371/journal.pone.0238606

Sibille, L., Carpenter, P., Systems, B., Schlagheck, R., & French, R. A. (2006, September). *Lunar Regolith Simulant Materials: Recommendations for Standardization, Production, and Usage* (NASA/TP—2006-214605). George C. Marshall Space Flight Center.

Srivastava, M., Rathee, S., Maheshwari, S., & Kundra, T. K. (2019). Design and processing of functionally graded material: review and current status of research. In L. Kumar, P. Pandey, & D. Wimpenny (Eds.), *3D Printing and additive manufacturing technologies* (pp. 243–255). Springer, Singapore

Suresh, S., & Mortensen, A. (1997). Functionally graded metals and metal-ceramic composites: Part 2 Thermomechanical behaviour. *International Materials Reviews*, *42*(3), 85–116. https://doi.org/10.1179/imr.1997.42.3.85

Taylor, S. R. (1987). The unique lunar composition and its bearing on the origin of the Moon. *Geochimica et Cosmochimica Acta*, *51*(5). https://doi.org/10.1016/0016-7037(87)90220-1

Tokita, M. (2003). Large-Size-WC/Co Functionally Graded Materials Fabricated by Spark Plasma Sintering (SPS) Method. *Materials Science Forum*, *423–425*, 39–44. https://doi.org/10.4028/www.scientific.net/msf.423-425.39

Vaniman, D., Reedy, R., Heiken, G., Olhoeft, G., & Mendell, W. (1991). The Lunar Environment. In G.H. Heiken, D.T. Vaniman, & B.M. French (Eds.), *Lunar Sourcebook: A User's Guide to the Moon*, Cambridge University Press, Cambridge, (pp. 27–60).

Wright, J. K., Evans, J. R. G., & Edirisinghe, M. J. (1989). Degradation of Polyolefin Blends Used for Ceramic Injection Molding. *Journal of the American Ceramic Society*, *72*(10), 1822–1828. https://doi.org/10.1111/j.1151-2916.1989.tb05985.x

Yakout, M., Elbestawi, M. A., & Veldhuis, S. C. (2020). A study of the relationship between thermal expansion and residual stresses in selective laser melting of Ti-6Al-4V. *Journal of Manufacturing Processes*, *52*, 181–192. https://doi.org/10.1016/j.jmapro.2020.01.039

Zhang, C., Chen, F., Huang, Z., Jia, M., Chen, G., Ye, Y., Lin, Y., Liu, W., Chen, B., Shen, Q., Zhang, L., & Lavernia, E. J. (2019). Additive manufacturing of functionally graded materials: A review. *Materials Science and Engineering: A*, *764*, 138209. https://doi.org/10.1016/j.msea.2019.138209

Zhang, X., Chen, Y., & Hu, J. (2018). Recent advances in the development of aerospace materials. *Progress in Aerospace Sciences*, *97*, 22–34. https://doi.org/10.1016/j.paerosci.2018.01.001

Zhang, X., Gholami, S., Khedmati, M., Cui, B., Kim, Y.-R., Kim, Y.-J., Shin, H.-S., & Lee, J. (2021). Spark plasma sintering of a lunar regolith simulant: effects of parameters on microstructure evolution, phase transformation, and mechanical properties. *Ceramics International*, *47*(4), 5209–5220. https://doi.org/10.1016/j.ceramint.2020.10.100

Zhang, X., Khedmati, M., Kim, Y.-R., Shin, H.-S., Lee, J., Kim, Y.-J., & Cui, B. (2019). Microstructure evolution during spark plasma sintering of FJS-1 lunar soil simulant. *Journal of the American Ceramic Society*, *103*(2), 899–911. https://doi.org/10.1111/jace.16808

Zheng, X., Deotte, J., Alonso, M. P., Farquar, G. R., Weisgraber, T. H., Gemberling, S., Lee, H., Fang, N., & Spadaccini, C. M. (2012). Design and optimization of a light-emitting diode projection micro-stereolithography three-dimensional manufacturing system. Review of Scientific Instruments, 83(12), 125001. https://doi.org/10.1063/1.4769050